Energy Technology
Generation, Conversion, Storage, Distribution
www.entechnol.de

Molybdenum Dichalcogenide Cathodes for Aluminum-Ion Batteries

*Shalini Divya, James H. Johnston, and Thomas Nann**

Many successful battery electrodes are based on 2D-layered materials. Aluminum-ion batteries are studied using molybdenum dichalcogenides: MoS_2, $MoSe_2$, and MoSSe as active cathode materials. The batteries show clear discharge voltage plateaus in the ranges 1.6–1.4 V for MoS_2 and $MoSe_2$, and 0.6–0.5 V for MoSSe. MoS_2 and $MoSe_2$ have similar crystal structures; interestingly, it is found that $MoSe_2$ performed better than MoS_2. MoSSe exhibits a higher specific capacity over MoS_2 and $MoSe_2$, but the energy density is lower than $MoSe_2$ at a current rate of 40 mA g^{-1}. $MoSe_2$ cells record a discharge capacity of ≈110 mAh g^{-1} with an average potential in the range of 2.0–1.8 V and 1.5–0.8 V during discharge. The cells are stable at 100 mA g^{-1} for over 200 cycles with 90% coulombic efficiency.

1. Introduction

Aluminum-ion batteries (AIBs) offer an alternative to the prevalent lithium-ion battery (LIB) technology. Aluminum being the most abundant metal in the Earth's crust, these batteries will not only be much cheaper, but hold promise to solve other problems such as recycleability and thermal runaway. Furthermore, the multivalent nature of aluminum may result in a higher specific capacity and energy density compared with other monovalent battery types. Research on AIBs is still in its early stages, and the current work focuses mainly on electrolytes and cathode materials. In this article, we explore different molybdenum dichalcogenide-based materials and their mechanism of energy storage. We expected that 2D-layered materials that support intercalation of charged species might be suitable as active cathode materials in AIBs.[1,2]

The most common AIB electrolyte is currently the ionic liquid 1-ethyl-3-methylimidazolium/tetrachloroaluminate ($[EMIm]^+/AlCl_4^-$), although many other alternatives are under investigation.[3] The most studied cathode types are graphite-based, where chloroaluminate ions $AlCl_4^-$ have been shown to intercalate/deintercalate during the charging/discharging processes. Various forms of graphite such as fluorinated graphite,[4] Kish graphite flakes,[5] 3D graphitic foam,[6] few-layer graphene aerogels,[7] and several others have been tested. Analytical techniques such as X-ray diffraction (XRD), Raman spectroscopy, and X-ray photoelectron spectroscopy (XPS) have been used broadly to verify the intercalation/deintercalation mechanism.

Molybdenum dichalcogenides (MoX_2 where X = S, Se, or Te) display similar properties as graphite. They have a 2D-layered structure, which allows intercalation of ions and is electrically conductive. Lower volumetric expansion on cycling is an advantage these materials have over graphitic cathodes.[8,9] Among various transition metal chalcogenides, MoS_2 has been extensively studied as a cathode for rechargeable batteries,[10–13] making them attractive candidates for AIB cathodes. In 2015, Geng et al. found that Al^{3+} ions fully intercalated into chevrel phase Mo_6S_8 with the cations occupying two different sites in the crystal lattice.[14] This mechanism was called the "rocking chair" mechanism where charge-carrying species shuttled back and forth between intercalating electrodes during cycles, whereas the overall electrolyte concentration remains constant. The discharging and charging reactions at the anode (Equation (1)) and cathode (Equation (2)) were proposed as follows:

$$Al + 7AlCl_4^- \rightleftharpoons 4Al_2Cl_7^- + 3e^- \quad (1)$$

$$8AlCl_7^- + 6e^- + Mo_6S_8 \rightleftharpoons Al_2Mo_6S_8 + 14AlCl_4^- \quad (2)$$

Three years later, Li et al. prepared MoS_2 microspheres by a simple hydrothermal method.[15] They proposed a similar mechanism where Al^{3+} ions inserted into the electrode accompanied by a phase transformation at the electrode interface. Li and his group confirmed this phase transition by using ex situ XPS and XRD etching techniques. The reaction equations for this battery system at the cathode (Equation (3)) and anode (Equation (4)) were proposed as follows

$$MoS_2 + xAl^{3+} + 3xe^- \rightleftharpoons Al_xMoS_2 \quad (3)$$

$$Al + 7xAlCl_4^- \rightleftharpoons 4xAl_2Cl_7^- + 3xe^- \quad (4)$$

In general, these cells showed low energy density and had reversibility issues in the redox processes. It has been reported that transition metal dichalcogenide electrodes tend to transition

Dr. S. Divya, Prof. J. H. Johnston
School of Chemical and Physical Sciences
Victoria University of Wellington
PO Box 600, Wellington 6140, New Zealand

Prof. T. Nann
School of Mathematical and Physical Sciences
The University of Newcastle
Callaghan, NSW 2308, Australia
E-mail: thomas.nann@newcastle.edu.au

The ORCID identification number(s) for the author(s) of this article can be found under https://doi.org/10.1002/ente.202000038.

DOI: 10.1002/ente.202000038

from a 2H phase into a more conducting 1T phase when used in a battery.[16] A hybrid Mg^{2+}/Li^{+} cell was tested using bulk MoS_2 as a cathode material. During cyclic voltammetry (CV) scans, the authors associated the first cathodic peak, with a phase transition. 2H phase MoS_2 was converted to 1T phase during initial ion intercalation. This seems to be a common phenomenon for molybdenum dichalcogenides, since Li et al. observed similar transitions in sodium ion batteries.[17,18] It mostly takes place during the first cycle and because the phase change is irreversible, it can be detected in a cyclic voltammogram.

In this work, we studied a range of 2D molybdenum dichalcogenides including MoS_2, $MoSe_2$, and MoSSe, and tested them as cathodes for nonaqueous AIBs. Our unpublished, preliminary density functional theory (DFT) calculations indicated a significant decrease in interlayer spacing of these materials when Al^{3+} cations were assumed to intercalate (owing to the very high charge density of Al^{3+}). Therefore, we propose intercalation of structurally distorted $AlCl_4^-$ anions into the cathode layers. Surprisingly, we found that $MoSe_2$-based cathodes performed different and better than all of the other molybdenum dichalcogenides.

2. Results and Discussion

Figure 1 shows the crystal structure of MoX_2, where X is sulfur (S) and/or selenium (Se). The material has two vacant sites for intercalation—M1 and M2. M1 denotes the spaces in between the X–Mo–X atoms, whereas M2 represents the space created between the MoX_2 layers, as shown in Figure 1a. The interlayer distance in MoX_2 is 6.3 Å with a gallery height of 3 Å. The layers are held together by weak van der Waals (vdW) forces. M2 presents an open network and provides various interstitial sites for intercalation. As $AlCl_4^-$ ions are 5.28 Å in diameter, as reported by Takahashi et al.,[19] they undergo some distortion during intercalation to fit into these layers. Our preliminary results showed that Al^{3+} would contract the MoX_2 layers when trying to intercalate, making $AlCl_4^-$ anion intercalation more likely. Also, the triply charged Al^{3+} cation has to overcome strong electrostatic forces from the S^{2-} or Se^{2-} anion network to enter, making the intercalation process slow and most likely not reversible. Therefore, we propose intercalation of $AlCl_4^-$ anions from the electrolyte into M2 sites of MoX_2 during charge. Galvanostatic cycles, CV, XRD, Raman spectra, and XPS results discussed later, strongly support our claim of a reversible intercalation process especially in $MoSe_2$.

A modified two-electrode polyether ether ketone (PEEK) cell (**Figure 2**) was used for conducting preliminary electrochemical tests. Cathode preparation, electrolyte synthesis, and cell configuration are described in Section 4.

Figure 3a–c shows the charge/discharge cycles (CDCs) for MoS_2, $MoSe_2$, and MoSSe at a current rate of 40 mA g^{-1}. The discharge capacity of MoS_2 in its first cycle was found at ≈45 mAh g^{-1} (Figure 3a). Comparing this with its first CV scan (Figure 3a, inset), a good correlation between the discharge voltage plateau and reduction peaks, and other redox features was found. The voltage bend during discharge at 2.0 V matched well with the reduction peak at 2.0 V. The other reduction peak at 1.0 V, however, did not correspond to any of the other peaks.

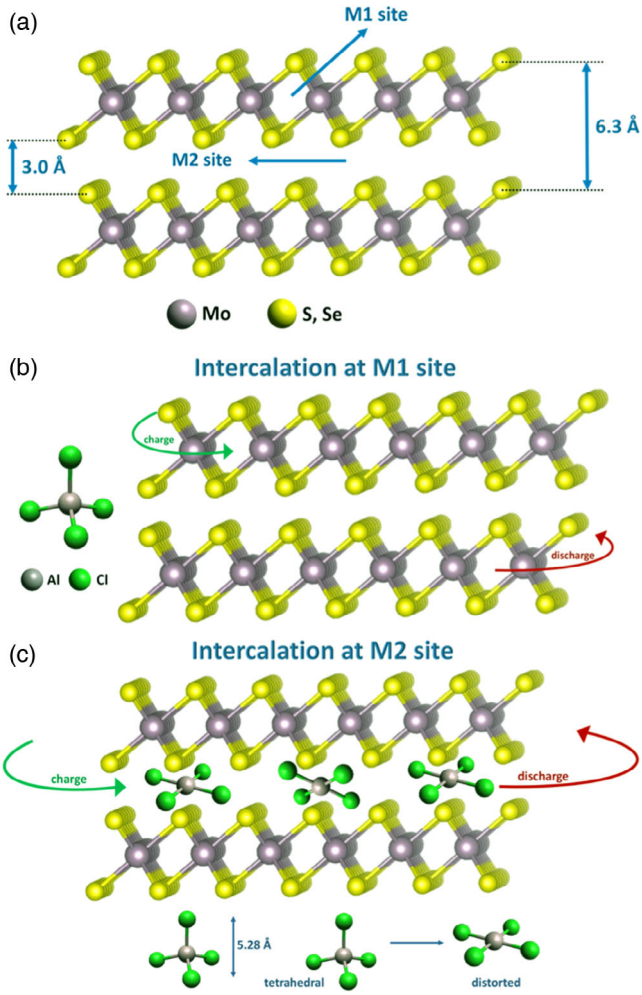

Figure 1. Schematic representation of a) a MoX_2 crystal structure with possible intercalation sites at M1 and M2; b) intercalation at M1 site; and c) intercalation at M2 site.

With discharge voltage bends between 2.0–1.8 and 1.5 −0.8 V, the first CV scan for $MoSe_2$ displayed two reduction peaks at 1.65 V (point A) and 1.0 V (point B) (Figure 3b, inset). The peak at 1.0 V suggested an irreversible reaction because this peak was absent in the following scans. Based on this, we agree with Li et al.'s interpretation and attributed this peak to an irreversible phase transition.[17] During this transition, the semiconducting 2H phase converted into a more metallic 1T phase. This transition seemed to increase the interlayer spacing of $MoSe_2$ by reducing the vdW forces that exist between the two layers.[16] Al/MoSSe cells showed three distinct plateaus during charge at 1.2, 2.0–2.1, and 2.3–2.4 V in its first cycle, with a discharge plateau at 0.5 V, as shown in Figure 3c. Capacities of all molybdenum dichalcogenides were recorded at different current rates of 25, 40, and 100 mA g^{-1}, and shown in Figure 3d. As $MoSe_2$ displayed stable specific capacities at all current rates, we recorded further 200 cycles at a high current rate of 100 mA g^{-1}. A highly reversible electrochemical reaction was observed because the capacity remained at ≈35 mAh g^{-1} after 200 cycles (Figure 3e) at 100 mA g^{-1}. The presence of multiple

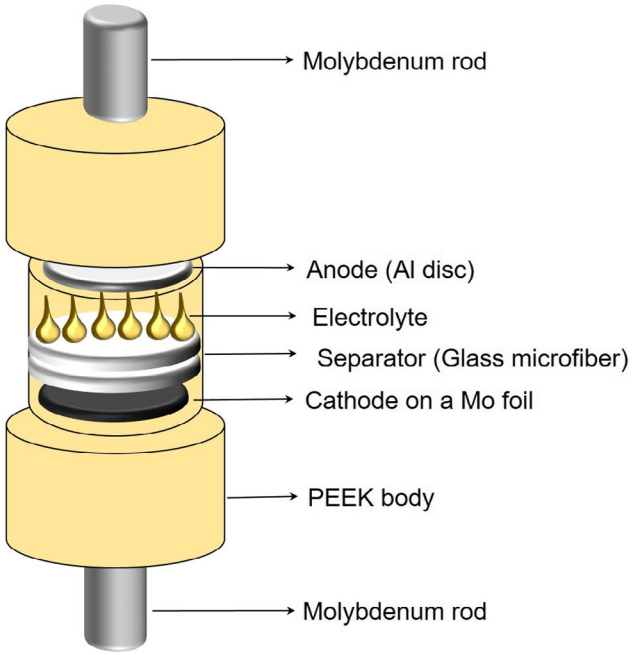

Figure 2. Two-electrode cell assembly using a customised PEEK body. Molybdenum (Mo) foil was used as the current collector with cathode material coated on top (working electrode) and Mo rods acted as plungers in this Swagelok-type cell. Glass microfibers were used as separators with 99.99% pure Al foil used as anode.

charging plateaus in MoSSe might correspond to various oxidation processes occurring when $AlCl_4^-$ interacts individually with S and Se atoms. The first CV scan (Figure 3c, inset) showed an irreversible reduction potential at 0.9 V, point B′, like $MoSe_2$, implying a similar phase transition. It seems MoSSe undergoes a lattice distortion and the material loses its long-range order after converting to its 1T phase. This might be the reason why the cells fail to deliver a stable capacity. In addition, a significant difference was observed charge/discharge curves of all the molybdenum dichalcogenide cathodes—similar to what was previously reported by Li et al. in 2018.[15] Electrochemical polarisation at the electrode interface might be responsible for the uneven potentials. Formation of an insulating layer on the cathode surface by the new Al–MoX_2 complexes might have attributed to the overpotential.

Electrochemical performance of a blank cell with an uncoated Mo foil (Figure S11, Supporting Information) showed that the current collector did not contribute to the cell's capacity. Both MoS_2 and $MoSe_2$ have similar interlayer distance (6.3 Å) and a gallery height of 3.0 Å. However, $MoSe_2$ showed a higher capacity and a more stable cycle life. To account for this behaviour, we compared the CVs of all electrodes at a scan rate of 10 mV s^{-1}, as shown in **Figure 4**. Different charge storage mechanisms lead to distinct features in the CVs. Ideal capacitors result in a rectangular CV shape. Due to the absence of Faradaic processes, the charging/discharging currents become directly proportional to the scan speed. Batteries show oxidation and reduction peaks in their voltammograms because the charge storage takes place via reversible redox processes.[20] We observed that the CVs of $MoSe_2$ and MoSSe in Figure 4b,c covered a broader area, suggesting an additional capacitor-like charge storage mechanism. The non-Faradaic process taking place at the surfaces of $MoSe_2$ and MoSSe might have added to their original capacity values. Also, the peak indicating phase transition from 2H → 1T at ≈0.9–1.0 V was visible only for $MoSe_2$ and MoSSe. Therefore, it can be concluded that the charge storage in MoS_2 is primarily based on reversible oxidation and reduction of Mo from Mo^{4+} to Mo^{5+} with oxidation peaks visible at 1.8 V (O1) and 2.1 V (O2), and a corresponding reduction peak at 2.0 V (R3) (Figure 4a). Two more reduction peaks were found at 1.6 V (R2) and 0.9 V (R1). However, their peak intensities decreased with every scan. CV scans of Al/$MoSe_2$ cells in Figure 4b indicated a reversible electrochemical process, which was in agreement with their CDCs. The scans overlapped with each other displaying two oxidation peaks at 1.7 V (O′1) and 2.1 V (O′2) and corresponding reduction peaks at 1.8 V (R′1) and 1.6 V (R′2). In Figure 4c, an oxidation and a reduction peak at 1.7 V (O″1) and 1.8 V (R″1) was observed for Al/MoSSe, respectively. R″1's peak intensity increased after every scan, which might suggest sluggish kinetics in the system—perhaps due to strong interaction between the positive metal ion and the intercalating anion. The voltammogram became more capacitor-like after a few scans, indicating the absence of reversible redox processes. The phenomena indicate that an initial intercalation of anions into the layers of MoSSe was followed by surface adsorption of $AlCl_4^-$ anions.

Figure 5 shows the XRD patterns of MoS_2, $MoSe_2$, and MoSSe electrodes. Pristine (in black), charged (in green), and discharged (in red) cathodes were compared after 30 cycles each. MoS_2 cells displayed a very small shift in their d-spacings. The peak at 14.21° for 002 plane (6.22 Å) shifted to 14.02° (6.32 Å), as shown in Figure 5a. Most of the peaks retained their positions after charge and discharge showing no significant change in the lattice dimensions. A completely different XRD pattern appeared after charging for Al/$MoSe_2$ cells, as new peaks appeared at 2θ values, as shown in Figure 5b. Diffraction peaks of 002, 100, 110, and 008 planes reappeared after discharge. Every time the cells were charged, $MoSe_2$ seemed to adopt this new crystal lattice. However, the characteristic peaks of $MoSe_2$ reappeared after discharge. This follows closely the observations made by Rani et al., where they proved intercalation of ions into the layers of fluorinated natural graphite during charging using XRD data.[4] This strongly confirms our hypothesis of a reversible intercalation taking place in $MoSe_2$. It was interesting to note that MoSSe did not have a well-defined crystal structure to begin with (Figure 5c). The patterns after charge and discharge did not look any different from the untested cathode. This confirmed MoSSe layers did not undergo any significant expansion and the initial specific capacities at ≈250 mAh g^{-1} came from the non-Faradaic reactions via electrostatic absorption of the $AlCl_4^-$ anions onto the electrode's surface. Furthermore, the material underwent irreversible changes resulting in cathode degradation after a few cycles. The images obtained from the scanning electron microscope (SEM) have been shown in Figure S12, Supporting Information. While MoS_2 and $MoSe_2$ displayed a layered structure in Figure S12a,b, Supporting Information, respectively, MoSSe lacked a long-range order. The diffraction patterns of all the Al–Mo–Se complexes present in the International Centre for

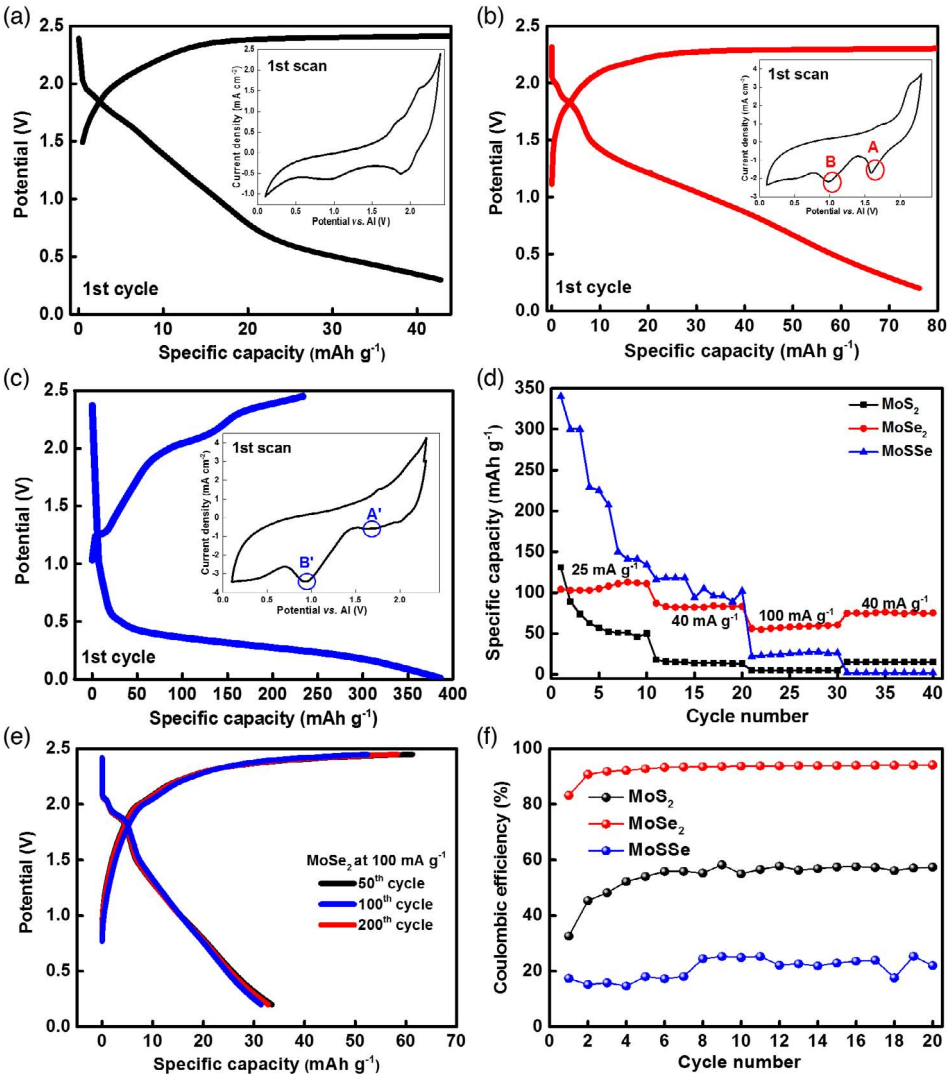

Figure 3. First charge/discharge curve at 40 mA g^{-1} for a) MoS_2, inset: first CV scan of MoS_2; b) $MoSe_2$, inset: first CV scan of $MoSe_2$; and c) MoSSe, inset: first CV scan of MoSSe at a scan rate of 10 mV s^{-1} versus Al/Al^{3+} electrode. d) Specific capacities of MoS_2, $MoSe_2$, and MoSSe at current rates of 25, 40, and 100 mA g^{-1} and then again at 40 mA g^{-1} to test the capacity retention. e) Charge/discharge performance of $MoSe_2$ at a high current rate of 100 mA^{-1} for 200 cycles. f) Coulombic efficiencies of MoS_2, $MoSe_2$, and MoSSe at a current rate of 100 mA g^{-1}.

Diffraction Data (ICDD) database have been compared with the new complex shown in Figure 5.

To further understand the interactions between $AlCl_4^-$ and $MoSe_2$, we used XPS, which is a useful method for distinguishing various oxidation states and helps in identifying different polymorphs (2H and 1T).[16] The detailed narrow spectrum scans in **Figure 6** show the binding energies of Mo ($3d_{5/2}$ and $3d_{3/2}$ in Figure 6a,b) and Al 2p peaks for charged $MoSe_2$ (Figure 6c) and MoSSe electrodes (Figure 6d). In pristine $MoSe_2$, two peaks appeared at 229.1 and 232.2 eV corresponding to $3d_{5/2}$ and $3d_{3/2}$ (**Figure 7**a). Selenium displayed a doublet at 55.4 and 54.6 eV corresponding to Se $3d_{3/2}$ and $3d_{5/2}$, respectively (Figure 7c). Peak splitting in an XPS spectrum can indicate a phase change or a change in oxidation state of the said element. After charge, the peak for Mo 3d split into three doublets, indicating the presence of multiple oxidation states or phases of Mo (Figure 6a). Se 3d deconvoluted into four peaks after charge (Figure 7e), confirming the presence of more than one phase after charge. This was similar to observations made by Fan et al. where they used MoS_2/graphene cathode in a hybrid Mg^{2+}/Li^+ cell. Pristine electrodes of MoSSe contained Mo in more than one oxidation state, and provided evidence for the presence of both 2H and 1T polymorphs (Figure 7b). After charging, the width of peaks at 231.7 eV (Mo $3d_{5/2}$, in green) and 228.6 eV (Mo $3d_{3/2}$, in green) increased, as shown in Figure 6b. After comparing Figure 7d,f, we noted that the Se 3d spectrum deconvoluted into four peaks after charging the MoSSe cells. An increase in the peak width was observed for both Mo and Se binding energies. A new peak at ≈236 eV in Mo 3d spectra (in blue) for MoS_2, $MoSe_2$, and MoSSe electrodes was assigned to Mo^{6+} species typically present in molybdenum oxide, MoO_3.

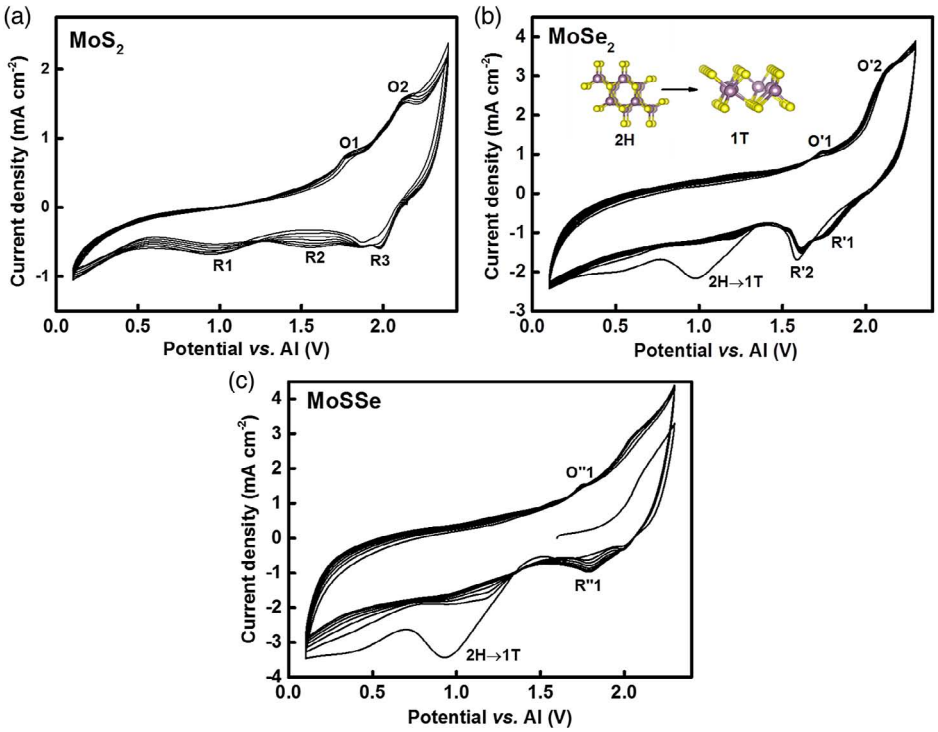

Figure 4. Cyclic voltammograms of a) MoS_2, b) $MoSe_2$, and c) MoSSe at a scan rate of 10 mV s^{-1} in a two-electrode aluminum-ion cell against an Al/Al^{3+} reference electrode.

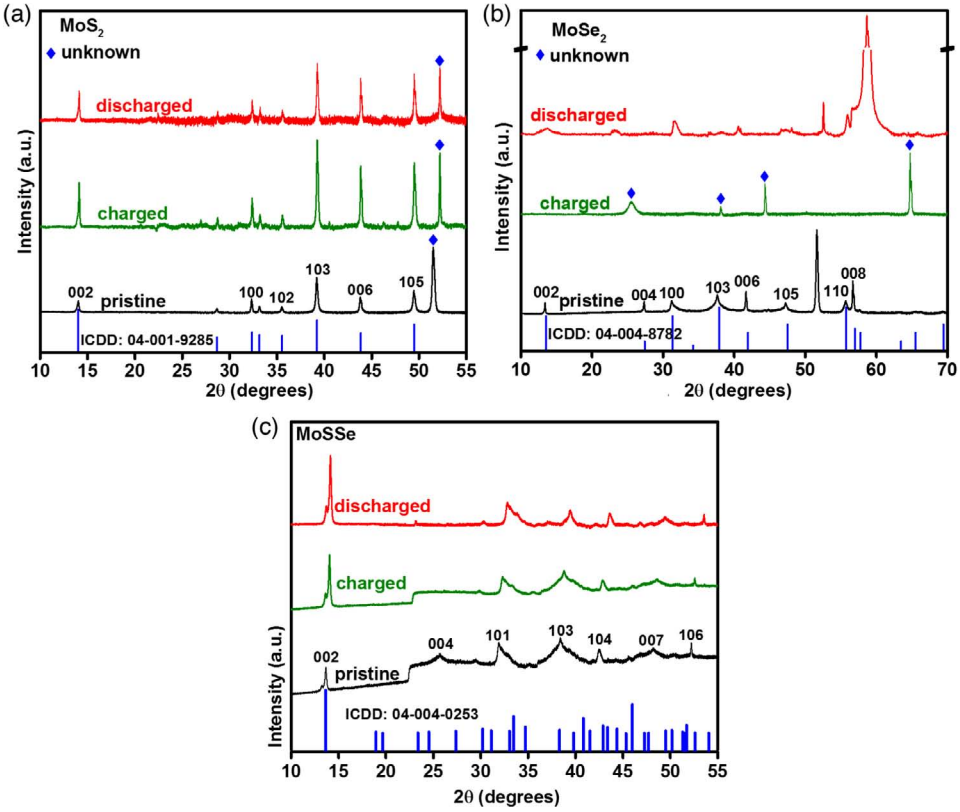

Figure 5. XRD patterns of pristine (black), charged (green), and discharged (red) a) MoS_2, b) $MoSe_2$, and c) MoSSe electrodes charged to 2.35 V and discharged to 0.2 V versus Al/Al^{3+}, with ICDD references, in blue.

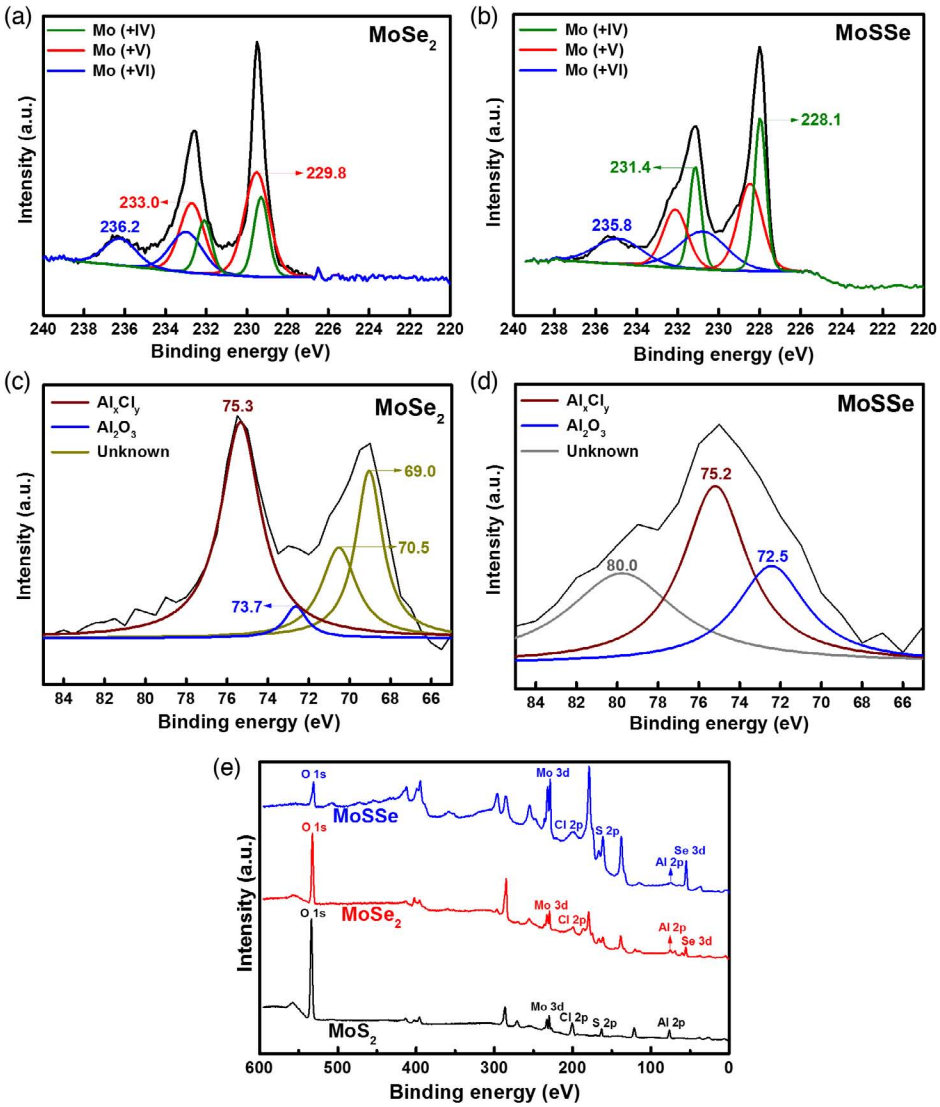

Figure 6. XPS spectra of Mo 3d orbitals in a charged a) $MoSe_2$ and b) MoSSe cathode and Al 2p orbitals in a charged c) $MoSe_2$ and d) MoSSe cathode. e) An overview spectrum of all three tested and charged cathodes.

The presence of new peaks and peak shifts that were detected in Mo 3d spectra for charged MoS_2 and $MoSe_2$ cathodes were not observed in MoSSe (cf. Figure 6a, 7a, and **8**a,b). This further confirms the absence of redox reactions and that the capacity was mainly derived from a surface-based charge storage. As expected, a general trend was observed for all the three cathodes, where the charged electrodes showed higher concentration of aluminum and chlorine than discharged electrodes, as shown in Figure 7g,h. The XPS spectra support the observation that $MoSe_2$ underwent a phase transformation that made it a better performing cathode than MoS_2. Further analysis is needed to fully understand the mechanism of MoSSe.

Charged $MoSe_2$ electrodes displayed binding energies of Al 2p at 77 eV (in red) and 76 eV (in blue) corresponding to chlorides Al_xCl_y and Al_2O_3, respectively, in Figure 6c. New peaks were observed at much lower binding energies—69 and 70 eV (in green) suggesting the presence of a new complex with an increased electron density around aluminum. An overall spectra of charged MoS_2, $MoSe_2$, and MoSSe cathodes is shown in Figure 6e, indicating the presence of Al and Cl (from chloroaluminates) and oxygen (from MoO_3).

In addition, we compared the Raman spectra of pristine and charged cathodes to detect shifts in vibrational modes shown in **Figure 9**. Yang et al. and Sharma et al. have reported that E^1_{2g} and A^1_g are the most intense vibrational modes for molybdenum dichalcogenides.[21–23] Peaks corresponding to E^1_{2g} and A^1_g modes for MoS_2 (Figure 9a) are prominent at 384.6 and 410.2 cm^{-1}, respectively. A^1_g indicates an out-of-plane symmetric displacement of S atoms, whereas E^1_{2g} suggests an in-layer displacement. Also, separation between the two peaks indicates a multilayer structure, which was observed for all three materials. No significant peak shift or peak broadening was observed for the charged MoS_2 electrode. For 2H $MoSe_2$ (Figure 9b), A^1_g is the most intense vibration occurring at a frequency lower than that

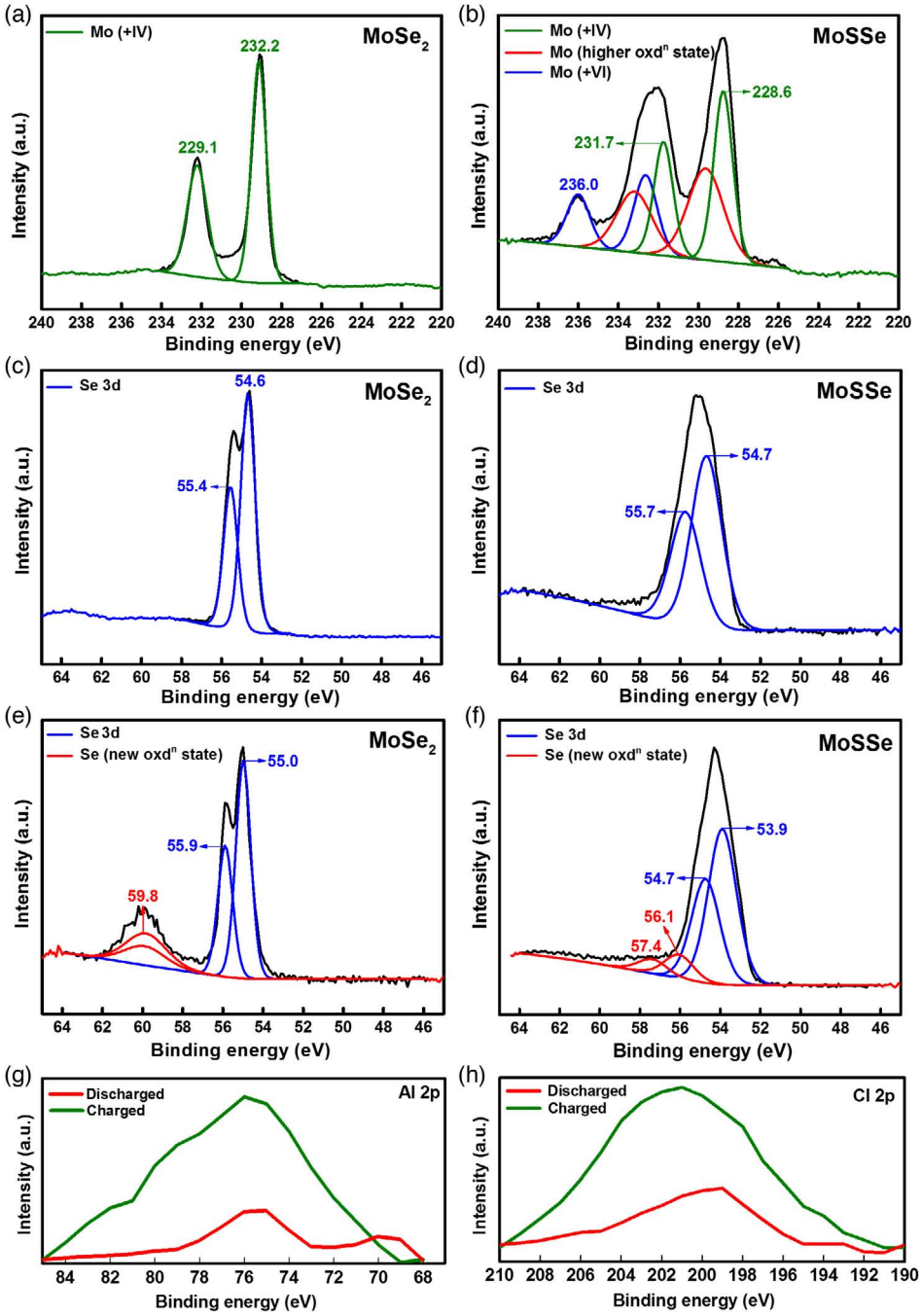

Figure 7. XPS spectra of Mo 3d for pristine a) MoS_2 and b) MoSSe electrodes. MoS_2 spectra consists of two peaks at 232.2 and 229.1 eV, corresponding to Mo^{4+}. MoSSe spectra consist of three doublet bands, which are assigned to Mo^{4+}, one with oxidation state between 4 and 6, and another band corresponding to Mo^{6+} at 236 eV. Se 3d orbital spectra for pristine c) $MoSe_2$ and d) MoSSe. Se from $MoSe_2$ observed peaks corresponding to $3d_{3/2}$ and $3d_{5/2}$ at 55.6 and 54.6 eV, respectively. Binding energies of Se 3d from charged e) $MoSe_2$ and f) MoSSe cathodes. Binding energies of g) Al 2p and h) Cl 2p in the charged and discharged cathodes—a general trend followed by all molybdenum dichalcogenides.

of E^1_{2g}. When the number of layers decreases, the A^1_g mode softens and an increase in full-width-at-half-maximum (FWHM) is detected. Spectra generated after intercalation were different from the pristine cathodes because phase conversion from 2H to 1T decreases the molecule's symmetry and more Raman bands get active. The presence of J1 and J2 peaks in addition to E^1_{2g} and A^1_g at lower wavelengths suggest the existence of 1T phase especially for $MoSe_2$ and MoSSe (inset, Figure 9b,c). This agrees with the CV scans and XPS results where a phase transition was observed for $MoSe_2$ and MoSSe. Raman results suggest that the symmetry and vibrational modes of $MoSe_2$'s crystal lattice changed after repeated cycles. It seems that the

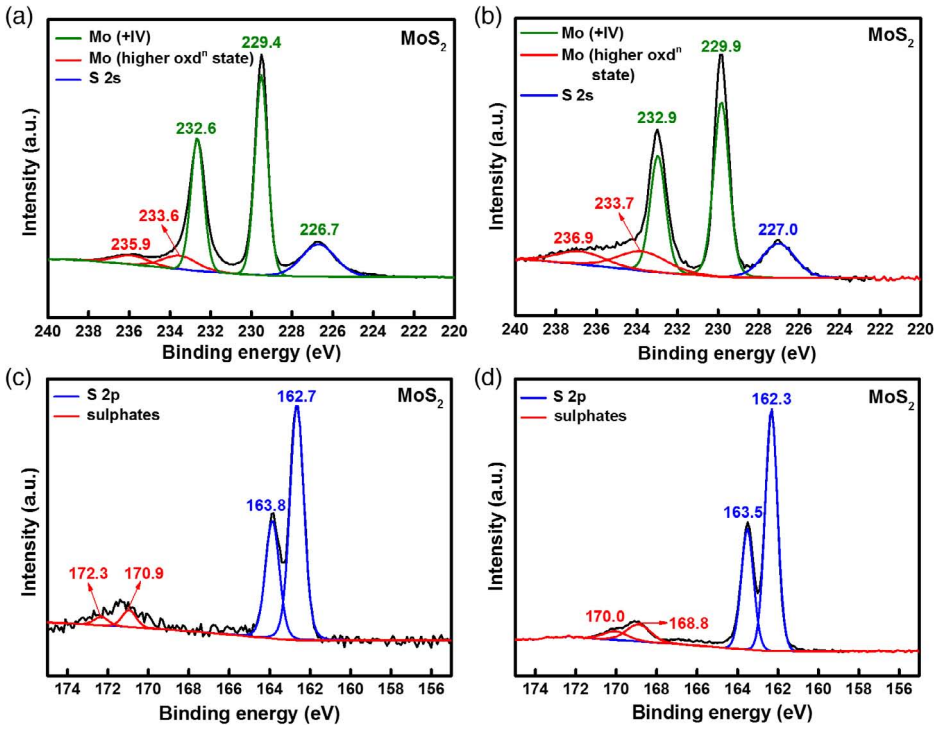

Figure 8. XPS spectra of Mo 3d and S 2s orbitals in a) a charged and b) discharged MoS_2 cathode and binding energies of S 2p orbital in c) a charged and d) discharged MoS_2 cathode.

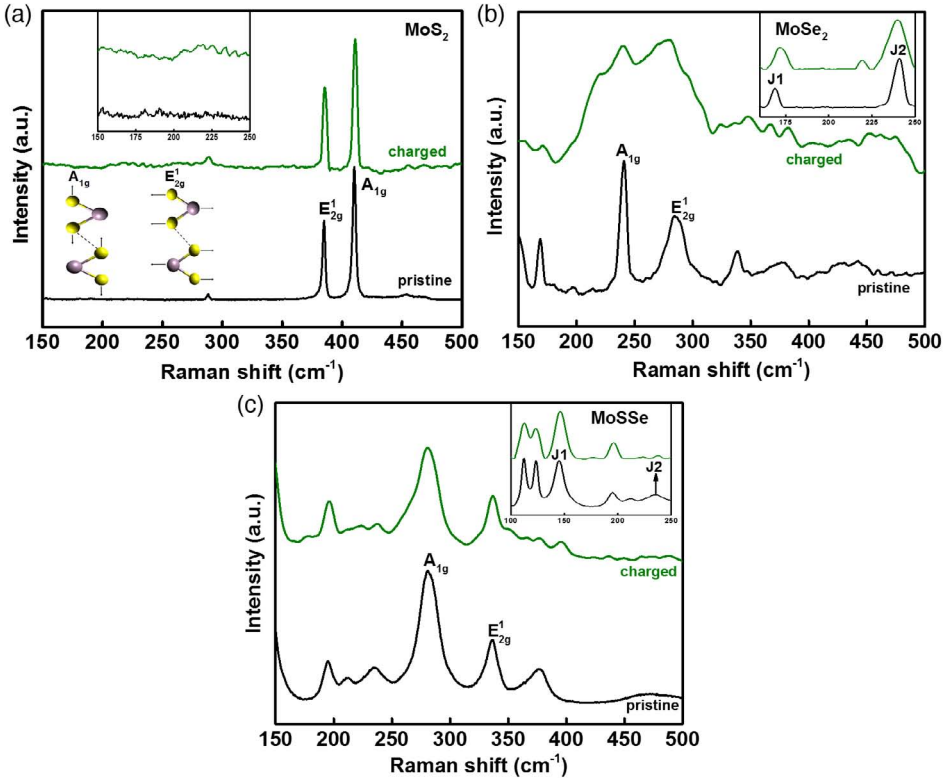

Figure 9. Raman spectra of pristine (black) and charged (green) a) MoS_2, b) $MoSe_2$, and c) MoSSe electrodes with position of new Raman active J1 and J2 bands marked along with E^1_{2g} and A^1_g bands.

phase transformation occurring in the first few cycles for $MoSe_2$ changes its structure in a way that allows it to intercalate more $AlCl_4^-$ anions resulting in a higher capacity than MoS_2 despite both of them having a similar stricture. First-principle studies on both materials shall confirm this hypothesis.

3. Conclusions

In this work, we studied systematically the charging/discharging mechanism of AIBs, using different molybdenum dichalcogenide cathodes. It was found that $MoSe_2$ showed a higher capacity and cyclic stability than MoS_2 and MoSSe. CV and XPS results indicated an irreversible phase transition to a more metallic 1T phase. This transition worked in favour of $MoSe_2$ and its capacity increased. XRD, XPS, and Raman results supported the hypothesis that $AlCl_4^-$ intercalated reversibly into $MoSe_2$. An additional electrocapacitive behaviour was observed in $MoSe_2$ that added to the its overall capacity. The cells delivered a potential of $\approx$2.0 V with discharge capacity of 30 mAh g^{-1} with nearly 95% coulombic efficiency at a current rate of 100 mA g^{-1}.

4. Experimental Section

Cathode Preparation: A slurry was prepared by mixing MoX_2 (85% by wt.), 9% binder (PVDF, MTI Corporation) and 6% Super-P conductive carbon (99+% metals basis, Alfa Aesar) in N-methyl pyrrolidone (NMP) (anhydrous, 99.5%, Sigma-Aldrich). This slurry was 'doctor-bladed' onto molybdenum foil (thickness 0.1 mm, MTI Corporation) and dried in a vacuum oven at 120 °C for 12 h to adhere the slurry on the conductive substrate and evaporate the solvent. The specific loading of the active materials was approximately 12 mg cm^{-1}.

Electrolyte Preparation: Anhydrous $AlCl_3$ (Sigma-Aldrich) and EMImCl (97%, Sigma-Aldrich) were mixed in a molar ratio of 1.3:1, at room temperature. EMImCl was baked in vacuum for 24 h at 100 °C to remove residual moisture. Small aliquots of $AlCl_3$ were added to EMImCl after every few minutes until the white fumes settled down. The ionic liquid was stirred for 2–3 h until a clear brown liquid was obtained. As the electrolyte was hygroscopic in nature, it was prepared in a N_2-filled glove box with $<$0.1 ppm H_2O/O_2.

Cell Assembly: PEEK cells were used for preliminary electrochemical tests. Molybdenum rods were used as plungers to push in the electrodes as close to each other. Active material coated on molybdenum foil was used as the cathode and placed at bottom of the cell. As this was a two-electrode setup, aluminum foil was used as both counter and reference electrode. We used Mo foil because nickel and steel showed reactivity toward the ionic liquid electrolyte and reduced its potential window. Glass microfibers (Grade GF/F, Whatman) were used as separators. An 80 µL of the electrolyte was used to wet the separator. Aluminum foil (thickness 0.1 mm, 99%, GoodFellow) was used as an anode and placed on top of the separator. The cell was then sealed and wrapped with a paraffin to avoid any further air or moisture contact after it was taken out of the glove box.

Supporting Information

Supporting Information is available from the Wiley Online Library or from the author.

Conflict of Interest

The authors declare no conflict of interest.

Keywords

aluminum-ion batteries, electrochemistry, layered compounds, molybdenum dichalcogenide cathodes

Received: January 9, 2020
Revised: March 9, 2020
Published online: April 22, 2020

[1] H. Zhang, *ACS Nano* **2015**, *9*, 9451.
[2] M. S. Whittingham, *Science* **1976**, *192*, 1126.
[3] N. Canever, N. Bertrand, T. Nann, *Chem. Commun.* **2018**, *54*, 11725.
[4] J. Vatsala Rani, V. Kanakaiah, M. Tulshiram Dadmal, Srinivasa Rao, S. Bhavanarushi, *J. Electrochem. Soc.* **2013**, *160*, A1781.
[5] S. Wang, K. V. Kravchyk, F. Krumeich, M. V. Kovalenko, *ACS Appl. Mater. Interfaces* **2017**, *9*, 28478.
[6] M.-C. Lin, M. Gong, B. Lu, Y. Wu, D.-Y. Wang, M. Guan, M. Angell, C. Chen, J. Yang, B.-J. Hwang, H. Dai, *Nature*, **2015**, *520*, 324.
[7] J. Qiao, H. Zhou, Z. Liu, H. Wen, J. Yang, *Ionics*, **2019**, *25*, 1235.
[8] Y. Liang, R. Feng, S. Yang, H. Ma, J. Liang, J. Chen, *Adv. Mater.* **2011**, *23*, 640.
[9] J. Huang, Z. Wei, J. Liao, W. Ni, C. Wang, J. Ma, *J. Energy Chem.* **2019**, *33*, 100.
[10] X.-L. Li, Y.-D. Li, *J. Phys. Chem. B* **2004**, *108*, 13893.
[11] C. Zhu, X. Mu, P. A. van Aken, J. Maier, Y. Yu, *Adv. Energy Mater.* **2015**, *5*, 1401170.
[12] S. Ding, D. Zhang, J. S. Chen, X. Wen (David) Lou, *Nanoscale* **2012**, *4*, 95.
[13] Y. Dong, Y. Xu, W. Li, Q. Fu, M. Wu, E. Manske, J. Kroger, Y. Lei, *Small* **2019**, *15*, 1900497.
[14] L. Geng, G. Lv, X. Xing, J. Guo, *Chem. Mater.* **2015**, *27*, 4926.
[15] Z. Li, B. Niu, J. Liu, J. Li, F. Kang, *ACS Appl. Mater. Interfaces* **2018**, *10*, 9451.
[16] X. Fan, R. R. Gaddam, N. A. Kumar, X. S. Zhao, *Adv. Energy Mater.* **2017**, *7*, 1700317.
[17] Y. Li, Y. Liang, F. C. Robles Hernandez, H. Deog Yoo, Q. An, Y. Yao, *Nano Energy*, **2015**, *15*, 453.
[18] M. Acerce, D. Voiry, M. Chhowalla. *Nat. Nanotech.* **2015**, *10*, 313.
[19] K. Takahashi, Y. Wang, G. Cao, *J. Phys. Chem. B* **2005**, *109*, 48.
[20] H. Jiao, J. Wang, J. Tu, H. Lei, S. Jiao, *Energy Technol.* **2016**, *4*, 1112.
[21] L. Yang, L. Dai, H. Li, H. Hu, K. Liu, C. Pu, M. Hong, P. Liu, *RSC Adv.* **2019**, *9*, 5794.
[22] C. N. R. Rao, W. Umesh Vasudeo, *2d Inorganic Materials beyond Graphene*, World Scientific, Singapore **2017**.
[23] C. H. Sharma, A. P. Surendran, A. Varghese, M. Thalakulam, *Sci. Rep.* **2018**, *8*.

